

Laser & Photonics Reviews / Volume 16, Issue 1 / 2100396

Research Article |  Full Access

Metasurface-Enabled High-Resolution Liquid-Crystal Alignment for Display and Modulator Applications

Jiawei Wang, Ke Li, Huilin He, Wengfeng Cai, Jianxun Liu, Zhen Yin, Quanquan Mu, Vincent K. S. Hisao, Davy Gérard, Dan Luo, Guixin Li, Yan Jun Liu 

First published: 15 November 2021

<https://doi.org/10.1002/lpor.202100396>

Citations: 2

[Get it @ NYU](#)

Abstract

Optical metasurfaces are 2D flat elements that consist of spatially arranged meta-atoms. By carefully designing the metasurface, it is possible to fully control the properties of light in amplitude, phase, and/or polarization. When merged with liquid crystals (LCs), a metasurface can act as a reconfigurable optical component enabling dynamical control of light. However, many reports ignore the influence of the meta-atom's geometry on the orientation of LCs. Here, it is proposed to synergistically merge LCs and specially designed gold metasurfaces for multiple optical functions. Gold metasurfaces are designed as a template to align the LC molecules in a resolution of $\leq 2 \mu\text{m}$. Meanwhile, the aligned LCs are used to actively control the polarization of the incident light, further achieving active modulation of the plasmonic resonances of gold metasurfaces. The synergistic mergence of LCs and metasurfaces can enable a designed optical device to work simultaneously in both visible and near infrared ranges, which is highly promising for multiple applications simultaneously, such as high-resolution display, modulation, anti-counterfeiting, beam deflection, LiDAR, etc.

1 Introduction

Optical metasurfaces allow an unprecedented control on the properties of light, including polarization [1-5], amplitude [6, 7] and phase [6-9] hence creating many interesting and exotic optical phenomena. However, most optical metasurfaces are only passive, lacking dynamic

control over their optical properties^[10-12] and hindering applications that require active/reconfigurable control of optical responses. Meanwhile, developing active optical metasurfaces has been also a longstanding goal, which can provide a new platform for reconfigurable and tunable optical devices.^[13-16] In particular, low-voltage tunable on-chip optical devices are attractive and even more competitive if they can achieve multifunctions at one time.^[6, 17-19] Recently, reconfigurable metasurfaces infiltrated with liquid crystals (LCs) have attracted significant attention.^[20-33] In addition, plasmonic metasurfaces can be also used as a photomask to further pattern the liquid crystal polymers.^[34, 35] As a gift of nature, LCs demonstrate remarkable optical properties including large birefringence, sensitive polarization-dependence, extremely broad spectral response, excellent biocompatibility due to their organic nature and versatile driving methods.

However, many reported works are only a juxtaposition of LCs and metasurfaces without considering the interaction between them. For instance, the alignment of LCs is a big concern in many LC-based metasurfaces. Irregular or highly symmetric (isotropic geometry) metasurface structures may be not able to provide perfect homogeneous alignment of LCs.^[36-39] An additional rubbing layer overlaid on the metasurface could align the LCs perfectly. However, mechanical rubbing may damage the metasurfaces, moreover, the addition of the alignment layer affects the interaction between LCs and metasurfaces significantly. Therefore, either direct combination or addition of alignment layer may deteriorate the optical performance of LC-based metasurfaces. Previous reports^[40-42] demonstrate that metastructures can help align the LC molecules, making a compact and integratable footprint. However, it is still challenging to unravel the alignment mechanism of the nanochannels or nanoholes in these reports. Moreover, they could also cause some alignment defects and nonnegligible scattering. Accordingly, a careful design consideration of LC alignment and metasurface structure is absolutely necessary.

In this work, we propose to synergistically merge LCs and gold metasurfaces with multiple purposes. We designed gold metasurfaces consisting of a periodic array of gold meta-atoms, which function as the alignment layer to align the LC molecules. Meanwhile, the aligned LCs are used to actively control the polarization of the incident light, further achieving active modulation of the plasmonic resonances of gold metasurfaces. By assembling the gold metasurface with another rubbed polyimide (PI)-coated substrate, a twisted nematic (TN) LC cell is formed. With the infiltration of nematic LCs, such a TN LC cell demonstrates high contrast of >300 in the visible range and a large modulation depth of $>45\%$ in the near infrared (NIR) range. Upon application of a driving voltage, the TN LC cell shows a clear switching effect in both visible and NIR ranges. Our proposed gold metasurfaces demonstrate much more improved performance including alignment, contrast, driving voltages, etc. More importantly,

Loading [MathJax]/jax/output/HTML-CSS/fonts/STIX-Web/Main/Regular/Main.js

metasurfaces can enable a designed optical device to work simultaneously in both visible and NIR ranges, which is highly promising for high-resolution display and optical modulator applications.

2 Results and Discussion

2.1 Design and Simulation

To efficiently synergize the LC and metasurfaces, we have specially designed the metasurfaces (see **Figure 1a**). It consists of periodic gold meta-atoms (nanorods), which exhibit different geometric anisotropies (i.e., different aspect ratios). Figure **1b** schematically depicts a single gold meta-atom located on an indium-tin-oxide (ITO) glass substrate. Each designed metasurface (i.e., the gold meta-atom array) has a period of $P = 600$ nm. The thickness of each metasurface is fixed to be $t = 50$ nm. The width of the gold meta-atom is set to be $W = 100$ nm, while its length (L) varies from 100 to 500 nm with a step size of 100 nm. Based on the above design, we simulated optical responses of the designed gold metasurfaces, as shown in Figure **1c–f**. With such a design, upon the normal incidence of light with different linear polarizations, the gold metasurfaces will demonstrate distinct optical responses, which are known as longitudinal (x -direction) and transverse (y -direction) modes due to the excitation of. [43] Moreover, the optical response of the gold meta-atoms is directly related to their size and shape, notably to the nanorod's aspect ratio (i.e., its W/L ratio). Figure **1c,e** shows the finite-difference time-domain (FDTD)-simulated transmission spectra (see Experimental Section for details) corresponding to the longitudinal and transverse plasmonic resonances of the gold metasurfaces, respectively. When $W/L = 1:1$, the meta-atoms are geometrically isotropic. As a result, both transverse and longitudinal resonances demonstrate indistinguishable optical responses at ≈ 792 nm. It is straightforward that plasmonic resonances tend to occur at relatively low energy (i.e., long wavelength) position. [44] Therefore, as the length L increases from 100 to 500 nm, the longitudinal resonance mode shows a distinct redshift from 792 to 1273 nm. In addition, the resonance becomes much stronger, showing a deeper dip on the transmission spectrum. According to Gans' formula, [45] the extinction cross-section C_{ext} for metallic nanorods can be calculated as follows:[46]

$$C_{\text{ext}} = 2 \pi V 3 \lambda \epsilon_m / 2 \sum_j (1/P_j^2) \epsilon_i (\epsilon_r + 1 - P_j P_j \epsilon_m)^2 + \epsilon_i^2 \quad (1)$$

where ϵ_m is the dielectric constant of the surrounding medium, ϵ_r and ϵ_i are the real and imaginary part of the dielectric function of the gold meta-atoms, V is the volume of the meta-atoms, P_j ($j = A, B, C$; A = length, B = width, C = thickness) are the depolarization factors for the meta-atoms which are given by

Loading [MathJax]/jax/output/HTML-CSS/fonts/STIX-Web/Main/Regular/Main.js

$$P_A = \frac{1 - e^2}{1 + e^2} \quad (2)$$

$$P_B = P_C = \frac{1 - P_A}{2} \quad \text{Assuming } B = C \text{ for simplicity} \quad (3)$$

where e is referred to as the meta-atom ellipticity given by $e^2 = 1 - \gamma^{-2}$, and γ is the aspect ratio of the meta-atom ($\gamma = A / B = \text{length} / \text{width}$).

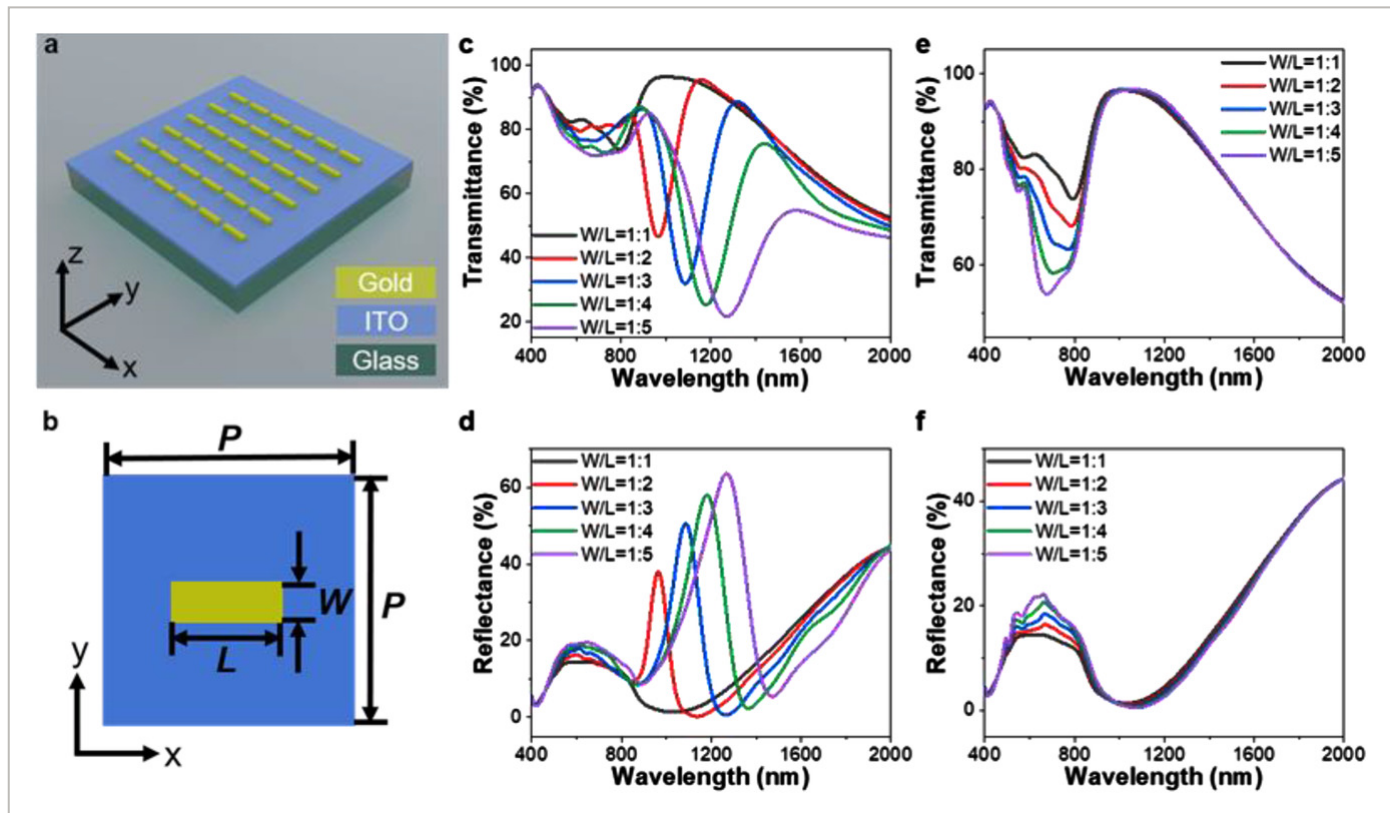


Figure 1

[Open in figure viewer](#) | [Download PowerPoint](#)

a) Schematic of the specially designed metasurface that consists of periodic meta-atoms. b) Details of geometric parameters of a meta-atom. c,e) Simulated transmission and d,f) reflection spectra of the designed bare metasurfaces with different aspect ratios of meta-atoms under the normal incidence of x- (c,d) and y-polarized (e,f) light, respectively.

The LSPRs occur when $\epsilon_r = -1 - P_j P_j \epsilon_m$, where $P_j = P_A = P$ length for the longitudinal mode and $P_j = P_B = P$ width for the transverse mode. For the gold meta-atoms with fixed thickness and width but different length, it finds that the longitudinal mode will continuously red-shift as the aspect ratio of the nanorod increases. In contrast, the transverse resonance shows a mirror blue shift [46]. The calculated electric field distributions of a single meta-atom for different W/L are plotted at both longitudinal and transverse resonances, as shown in

Figure [S1](#) (see the Supporting Information). The electric field distributions indicate that both longitudinal and transverse modes are the localized surface plasmon resonances (LSPRs) that are excited by two orthogonal linearly polarized incident light, respectively. Correspondingly, Figure [1d,f](#) illustrates the simulated reflection spectra of the gold metasurfaces for both longitudinal and transverse resonances, showing the similar aforementioned behaviors.

2.2 Polarization-Dependent Metasurfaces

With the above designs, we carried out the nanofabrication using electron-beam lithography and further measured their optical spectra using a UV-vis-NIR microspectrophotometer.

Figure 2a–e shows typical scanning electron microscopy (SEM) images of the fabricated metasurfaces with different aspect ratios. We can see that the gold meta-atoms have a smooth surface and sharp edges, indicating a high-quality nanofabrication. Figure [2f–j,k–o](#) respectively shows the measured transmission and reflection spectra of the fabricated metasurfaces for both x- and y-polarized incident light. The experimental results are in excellent agreement with the simulation, as shown in Figure [S2](#) (see the Supporting Information). We can see that the fabricated metasurfaces have clearly observable transverse and longitudinal resonances. The longitudinal resonances vary significantly with the aspect ratio, while the transverse ones keep almost unaltered as the width of the meta-atoms has been fixed. Overall, the fabricated metasurfaces have not only high transmittance (at least >65%) in the whole visible range, but also strong polarization-dependent resonances in the NIR range. The polarization-dependent transmission difference (ΔT) can reach more than 80%, indicating a strong polarization-switching effect. Based on these advantageous features, one can design optical devices that work simultaneously in both visible and NIR ranges for multifunction purposes.

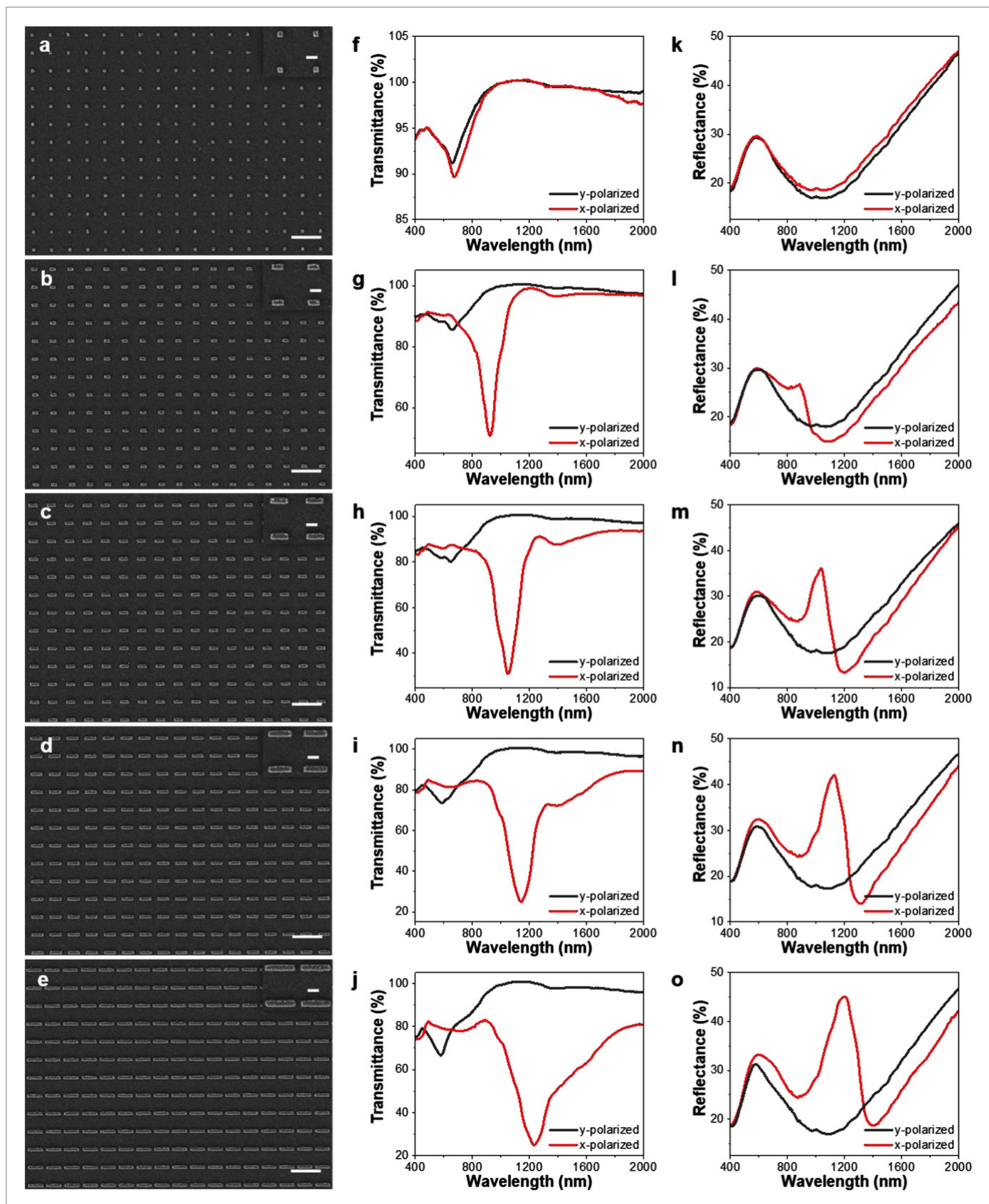


Figure 2

[Open in figure viewer](#)

 PowerPoint

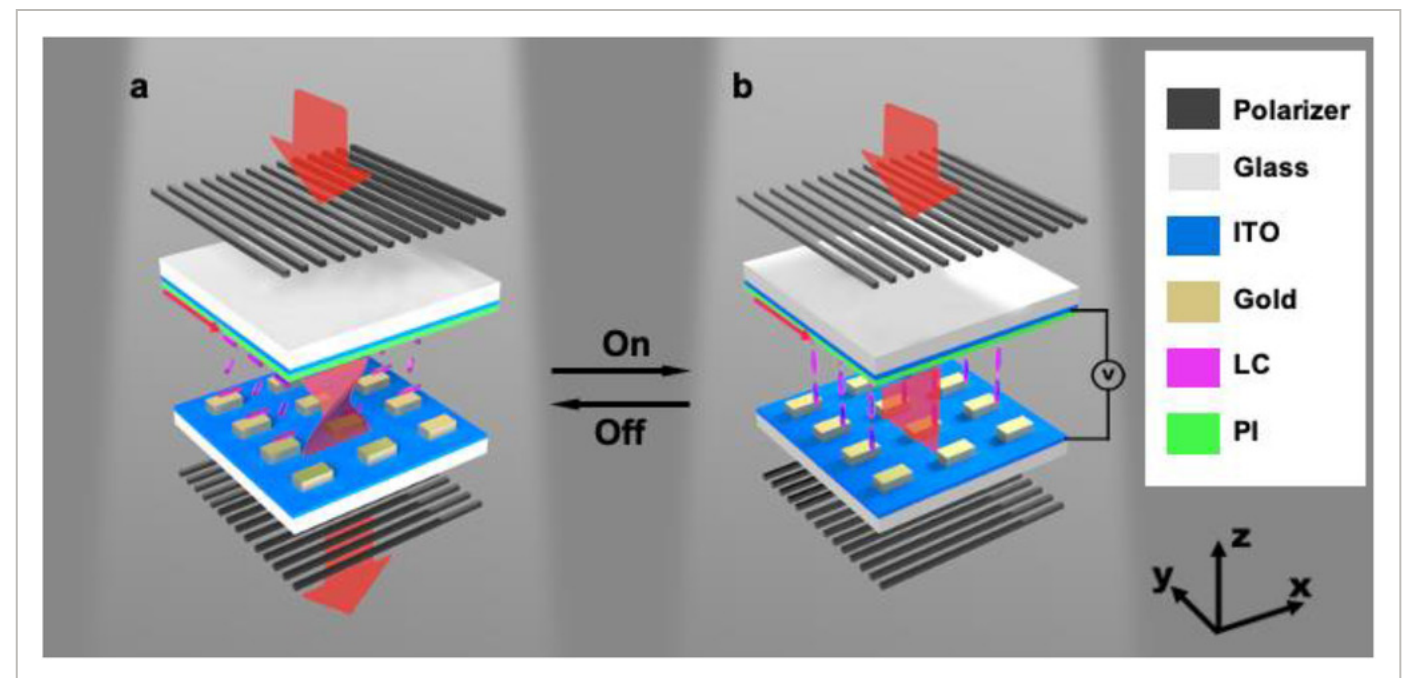
Loading [MathJax]/jax/output/HTML-CSS/fonts/STIX-Web/Main/Regular/Main.js

a–e) Typical SEM images of the fabricated metasurfaces with their meta-atoms having the aspect ratios of 1:1, 1:2, 1:3, 1:4, and 1:5, respectively. Scale bar: 1 μm . Insets are the magnified view of meta-atoms. Scale bar: 100 nm. f–j) Measured transmission and k–o) reflection spectra of the fabricated metasurfaces of the corresponding aspect ratios for x- (red lines) and y-polarized (black lines) incident light, respectively.

2.3 Tunable Metasurfaces and LC Alignment

In previous reports, we demonstrated that LCs can be well aligned on patterned nanostructures.^[47–49] We anticipate the same alignment behavior for LCs with the designed anisotropic metasurfaces, the anisotropy of the aligned meta-atoms enforcing the alignment of the LCs along the major axis of the nanorods. This principle is exemplified in **Figure 3**, which schematically shows a TN LC cell by assembling two pieces of the ITO-coated glass substrates (see details in the Experimental Section). It is worth mentioning that in our experiment, LCs were infiltrated into the cell at a temperature (65 °C) that was above their clearing point (59.6 °C). After infiltration, the LC cell was gradually cooled down to the room temperature. This means that during the infiltration, LCs were isotropic. There was no preferential alignment for the LC molecules. However, during the cooling process, LCs changed from isotropic to anisotropic, demonstrating a preferential alignment that was governed by the anchoring conditions provided by the metasurface layer at one side and the rubbed PI layer at the other side of the cell. As a result, the TN alignment was formed inside the cell. As the linearly y-polarized light is incident on the top surface of the TN cell (Figure 3a), during its propagation through the LC layer, the light polarization will rotate along the twist of LC director due to the well-known Mauguin effect.^[50] As a result, when the incident light reaches the bottom of the LC layer, the polarization of the incident light will rotate 90°, changing from y-direction to x-direction. Therefore, the metasurface will see the x-polarized light and the x-polarized light will then induce the longitudinal plasmonic resonance of the metasurface at the “Off” state. In contrast, upon electric switching (“On” state), all the LC molecules will realign along the electric field direction with no twist of the LC director. In such a case, for the same incidence of the linearly y-polarized light, the polarization of the light will be unaltered and it will not rotate anymore when propagating inside the LC layer. Therefore, the metasurface will see the y-polarized light and the y-polarized light will then induce the transverse plasmonic resonance of the meta-atoms array at the “On” state.

Loading [MathJax]/jax/output/HTML-CSS/fonts/STIX-Web/Main/Regular/Main.js

**Figure 3**
[Open in figure viewer](#) | [Download PowerPoint](#)

Schematic design of electrically tunable LC-loaded metasurfaces with a) 90° twisted and b) nontwisted LC layer at the “Off” and “On” states, respectively. The top ITO glass substrate is coated by a PI layer with the rubbing direction labelled by a red arrow. The metasurface situated on the bottom ITO glass substrate serves as both an alignment layer and a functional optical device simultaneously.

To validate our prediction, we first checked the LC alignment effect under polarizing optical microscopy (POM). **Figure 4** summarizes the observed results for different W/L ratios and POM configurations. Under two crossed polarizers, when the PI alignment direction is parallel to the optical axis of the polarizer, after the incident light passes through the LC layer, the polarization of the light will rotate 90°, which is hence parallel to the optical axis of the analyzer. Therefore, the incident light will pass through the analyzer and hence the patterned TN cell exhibits a bright state, as shown in Figure 4a. Upon applying a driving voltage of 20 V, the LC molecules will realign along the electric field direction. Hence, the polarization of the incident light is not altered, staying perpendicular to the optical axis of the analyzer. As a result, the incident light will be blocked by the analyzer and the TN cell exhibits a dark state, as shown in Figure 4b. The opposite effect can be clearly observable for the same TN cells under two parallel polarizers (see Figure 4c,d). It is worth noticing that the alignment effect of the designed metasurfaces is highly dependent on the W/L ratio of the meta-atoms. In the case of $W/L = 1:1$, the dark/bright contrast of the TN cell is almost indistinguishable, indicating that there is no preferential alignment of the LC molecules. This demonstrates that isotropic meta-atoms do not act as a

Loading [MathJax]/jax/output/HTML-CSS/fonts/STIX-Web/Main/Regular/Main.js increases (and hence the anisotropy of the meta-atoms increases), the alignment effect of the metasurfaces for the LC

molecules becomes stronger, which can be observed via the dark/bright contrast of the TN cells. These observed POM images confirm that the geometrically anisotropic gold meta-atoms are able to align the LC molecules. It is worth mentioning that some undesired features appear in the non-metasurface area, which are the defects occurred during the lift-off process. However, these defects do not affect the alignment performance of the measurfaces. With careful control of the fabrication processes, these defects can be completely avoided.

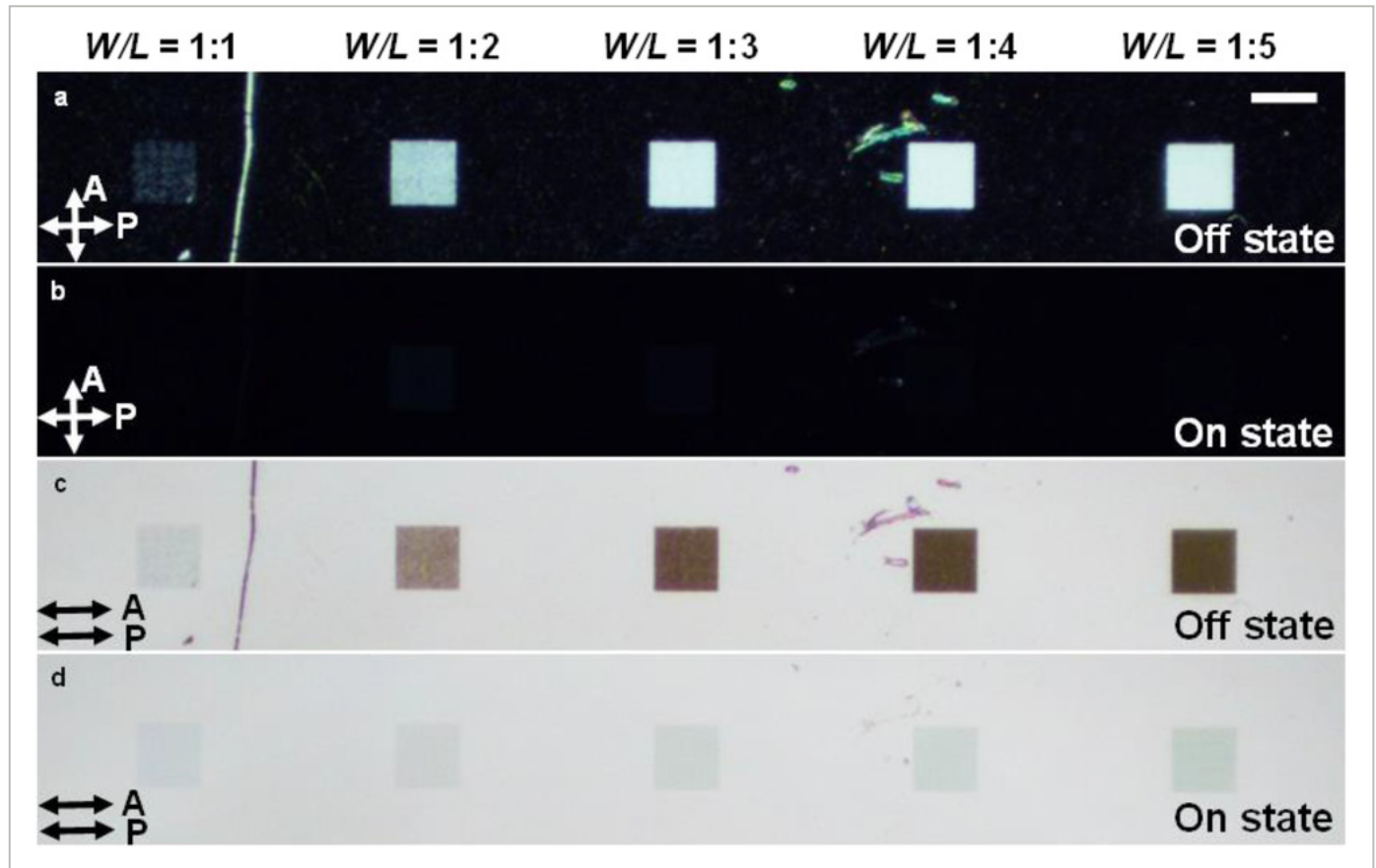


Figure 4

[Open in figure viewer](#) | [Download PowerPoint](#)

Typical POM images of the metasurface-based TN LC cell with the aspect ratios of $W/L = 1:1, 1:2, 1:3, 1:4$, and $1:5$, from left to right of each image under a,b) two crossed and c,d) parallel polarizers at the “Off” (a,c) and “On” (b,d) states, respectively. The driving voltage at the “On” state is 20 V. Scale bar: 100 μm .

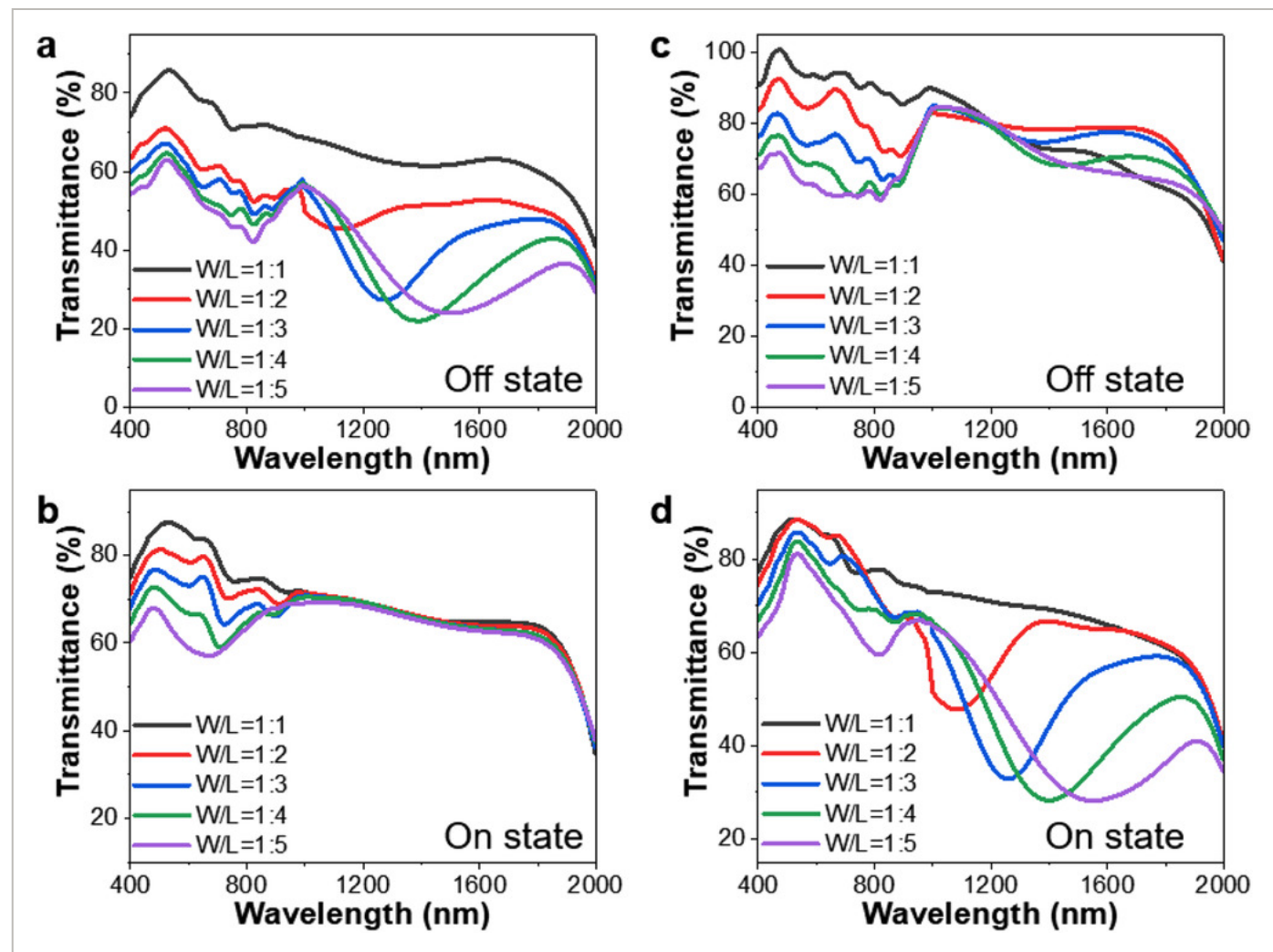
Furthermore, we spectrally evaluated the performance of the LC-loaded metasurfaces in terms of alignment and resonance modulating capability. In order to reduce the interference effect caused by the LC cell, we measured the transmission spectra of the LC cell using a small tilt angle.^[40] We set that the linearly polarized light is incident on PI-coated ITO glass substrate with the polarization parallel to the PI alignment direction. **Figure 5a** shows the measured

Loading [MathJax]/jax/output/HTML-CSS/fonts/STIX-Web/Main/Regular/Main.js e clearly observed that the LC-

loaded metasurfaces demonstrate a strong longitudinal plasmonic resonance. As known, LSPRs of the plasmonic nanoparticles are highly sensitive to the surrounding media.^[44] Therefore, we can observe that after the LC infiltration, the refractive index of the surrounding medium increases significantly, causing a large red shift in both the transverse and longitudinal modes compared to the bare metasurfaces (see Figure [S3](#) in the Supporting Information).

Experimentally, the transmission dip reaches $\approx 25\%$ when $W/L = 1:4$. Upon applying a voltage, reorientation of the LC molecules occurs and the transmission dip gradually disappears (see Figure [S4a-d](#) in the Supporting Information). In our experiments, we found that with an applied voltage of 7 V, the transmission dip completely disappeared, indicating that the LC molecules were fully realigned along the electric field direction, as shown in Figure [5b](#). In such a case, the light polarization does not change and the longitudinal plasmonic resonances are switched off. Instead, the transverse plasmonic resonances (corresponding to a shorter wavelength range) appear on the transmission spectra. An opposite behavior is observed when the polarization of the incident light is perpendicular to the PI alignment direction, as shown in Figure [5c,d](#).

Therefore, we can see that the LC-loaded metasurfaces significantly modulate the transmission (up to $\Delta T = 45\%$ or 4.8 dB in modulation depth) in the NIR range and meanwhile keep a high transmission in the visible range. Moreover, by switching the orientation of the LC molecules, the longitudinal and transverse plasmonic resonances can be interchanged.

**Figure 5**
[Open in figure viewer](#) | [PowerPoint](#)

Measured transmission spectra of the metasurface-based TN LC cell with the meta-atoms of different aspect ratios at the a,c) “Off” and b,d) “On” states for the linearly polarized incident light with the polarization a,b) parallel and c,d) perpendicular to the rubbing direction of the PI layer. The driving voltage at the “On” state is 7 V.

The electro-optical properties of the TN cells were further investigated in between two crossed polarizers. **Figure 6a** shows the dynamic responses of the transmission when a driving voltage was applied to the LC cell. We can see from Figure 6a, both threshold (V_{th}) and switching (V_s) voltages of the TN LC cell are highly dependent on the W/L ratios. The threshold and switching voltages tend to decrease as the W/L ratio decreases. As the aspect ratio of the meta-atoms varies from $W/L = 1:2$ to $W/L = 1:4$, the LCs’ orientation order gradually increases, resulting in reduced threshold and switching voltages. When $W/L = 1:5$, the anchoring energy of the metasurface might increase, resulting in an increase in the threshold and switching voltages as well. The measured V_{th} and V_s are ≈ 2 and ≈ 4 V when the length of the meta-atoms is larger than $10 \mu m$.

Loading [MathJax]/jax/output/HTML-CSS/fonts/STIX-Web/Main/Regular/Main.js | PI-based LC alignment systems. [31]

The derived contrast ratio ($CR = T_{\max} / T_{\min}$) can reach more than 300:1. The measured V_{th} , V_s , $CR@Vis$, and $\Delta T@NIR$ for the metasurface-based TN LC cells with different W/L ratios are summarized in Table 1 in detail. Figure 6b shows the measured rising and falling time for meta-atoms arrays area. Driven by square wave signals, the rising and falling times were captured. They were defined as the time intervals of the measured intensity change from 10% to 90% and 90% to 10%, respectively. With an applied voltage of 6 V, the optimal rising and falling times are 22 and 162 ms, respectively. It is worth mentioning that the falling time can be written as

$$\tau = \gamma_1 d^2 K_{22} \pi^2 \quad (4)$$

where γ_1 is the rotational viscosity of LCs, d is the LC cell gap, K_{22} is the elastic constant associated with twist deformation. From Equation (4), it is clear that the falling time is voltage-independent.

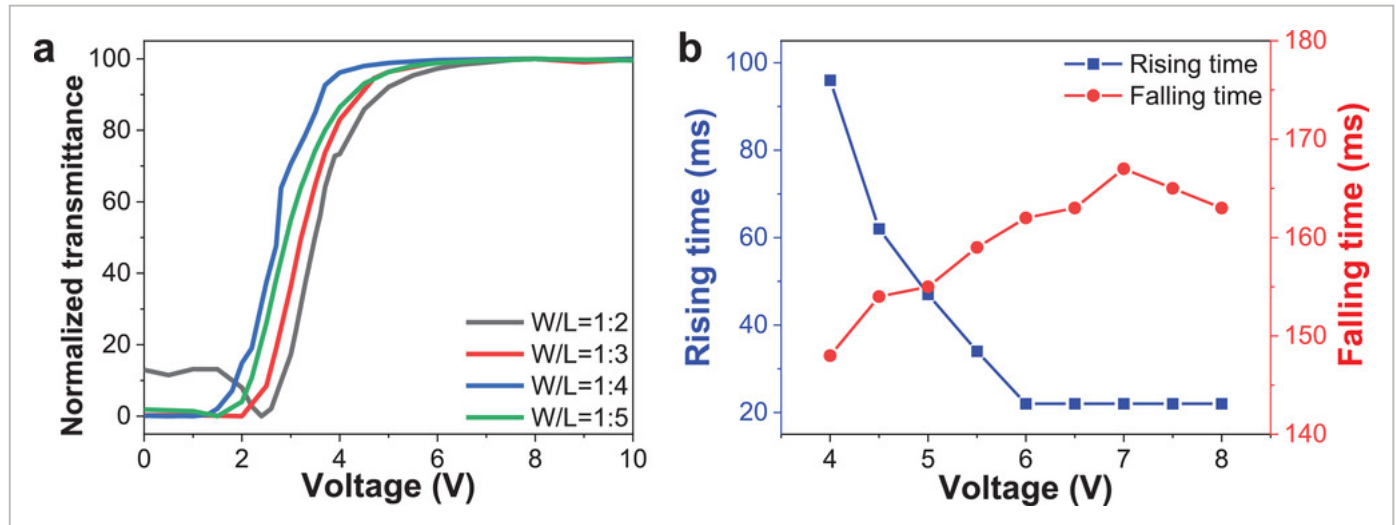


Figure 6

[Open in figure viewer](#) | [Download PowerPoint](#)

a) Normalized transmission curves as a function of the driving voltage of the metasurface-based TN LC cell with the meta-atoms of different aspect ratios. b) Measured rising and falling times as a function of the driving voltage.

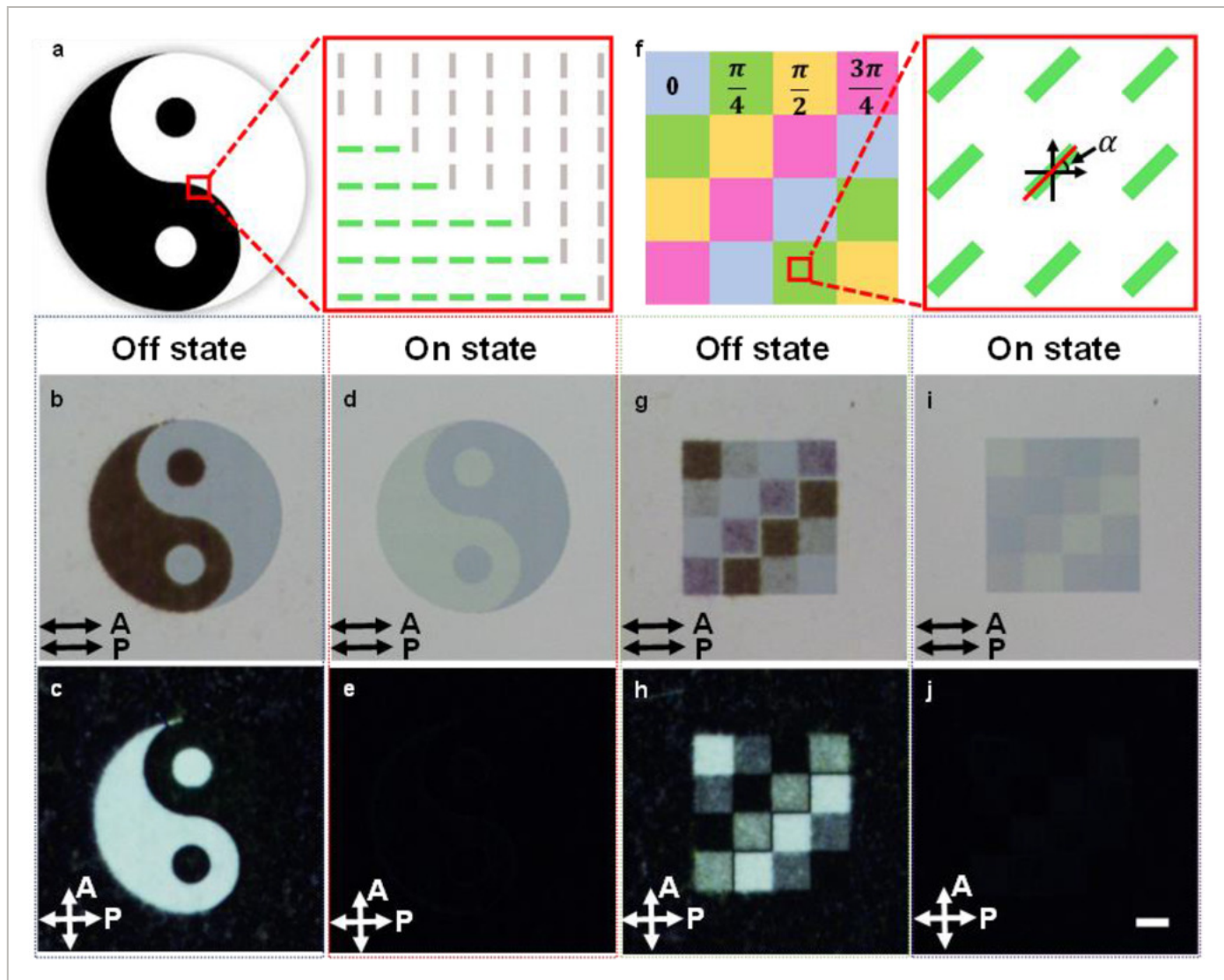
Table 1. Measured V_{th} , V_s , $CR@Vis$, and $\Delta T@NIR$ for the metasurface-based TN LC cell with different W/L ratios

W/L	V_{th} [V]	V_s [V]	$CR @ Vis$	$\Delta T[\%] @ NIR$
1:2	2.80	4.82	32.76	29.49

<i>W/L</i>	<i>V_{th}</i> [V]	<i>V_s</i> [V]	<i>CR @ Vis</i>	$\Delta T[\%]$ @ NIR
1:3	2.53	4.43	71.56	42.21
1:4	1.87	3.61	220.33	45.56
1:5	2.21	4.26	321.50	40.55

The synergistic mergence of LCs and metasurfaces is highly promising for high-resolution display and modulator applications. As a proof-of-concept, we have designed the Taiji and mosaic patterns, as shown in **Figure 7a,f**. The Taiji pattern consists of orthogonally arranged meta-atoms (see the SEM images in Figure **S5a,b** in the Supporting Information). The mosaic pattern has four typical segments of arranged meta-atoms with their orientation angles a from 0 to $3p/4$ at an interval of $p/4$ (see the SEM images in Figure **S5c-g** in the Supporting Information). The meta-atoms for both patterns have a fixed aspect ratio of $W/L = 1:4$. After assembling a TN LC cell, **Figure 7b-e,g-j** shows the POM images under two parallel and crossed polarizers at “On” and “Off” states. We can see that when the polarization of the incident light is changed, the bright and dark states can be exchanged, as shown in **Figure 7b,c**. Upon electric switching, the Taiji pattern can be totally reversed (comparing **Figure 7b,d**) or erased (a fully dark state, comparing **Figure 7c,e**). From the Taiji pattern, we can see clear, continuous boundaries, indicating that high-resolution LC alignment is formed. In the Taiji pattern, the orientation of the meta-atoms rotates abruptly over a sub-micrometer scale (see **Figure S5b** in the Supporting Information), and the LC molecules appear to be able to follow this abrupt change. This means that the orientation of the LC molecules is controlled with a high spatial resolution by the metasurface template. A more quantitative discussion is given below. More segments with gradually changed alignment can be also well observed from the mosaic pattern, as shown in **Figure 7g-j**. For examples, under the two crossed polarizers, the patterns with $a = 0$ are completely bright, while the patterns with $a = p/2$ are completely dark. The other patterns have the brightness in between the completely bright and dark states. The mosaic pattern was further investigated by rotating either the sample or the analyzer (see **Figure S6** in the Supporting Information), further confirming that the LC molecules can be well aligned locally. An eight-segmented metasurface pattern with eight orientation angles from 0 to 2π at an interval of $\pi/4$ was further designed for LC alignment. **Figure S7** (Supporting Information) shows the observed POM images, showing the high-quality, micrometer-scale localized alignment. In addition, we have recorded the real-time videos of all the fabricated patterns in this work under different configurations (see Videos **S1-S4** in the Supporting Information), which could provide more detailed dynamic information.

Loading [MathJax]/jax/output/HTML-CSS/fonts/STIX-Web/Main/Regular/Main.js

**Figure 7**
[Open in figure viewer](#) | [PowerPoint](#)

Schematically designed a) Taiji and f) mosaic patterns with orthogonally arranged and 4-level orientated meta-atoms, respectively. The used meta-atoms have the aspect ratio of $W/L = 1:4$. Corresponding POM images of the metasurface-based TN LC cell under two b,d,g,i) parallel and c,e,h,j) crossed polarizers at the “Off” (b,c,g,h) and “On” (d,e,i,j) states, respectively. Scale bar: 20 μm .

We have further investigated the alignment resolution of the designed metasurfaces. **Figure 8** demonstrates five designed square patterns with the meta-atoms of $W/L = 1:4$. Figure 8a shows the observed SEM images of the fabricated patterns with their sizes of 20, 15, 10, 5, and 2 μm^2 , respectively. From the POM images in Figure 8b,c, all the five patterns provide excellent alignment effect. The achieved resolution of alignment pixel is at least 2 μm^2 , which consists of only 16 meta-atoms. In our viewpoint, the main factors affecting the resolution are not only the

Loading [MathJax]/jax/output/HTML-CSS/fonts/STIX-Web/Main/Regular/Main.js } of the LC cell. In our experiment,

the cell thickness was 5 μm . If the cell thickness is further reduced, we believe the spatial resolution of the metasurface-aligned LCs can be significantly increased. However, it becomes challenging to resolve the alignment due to the limited resolution of the optical microscope. However, a 2 μm alignment resolution would be sufficient for most LC display or other optoelectronic applications.

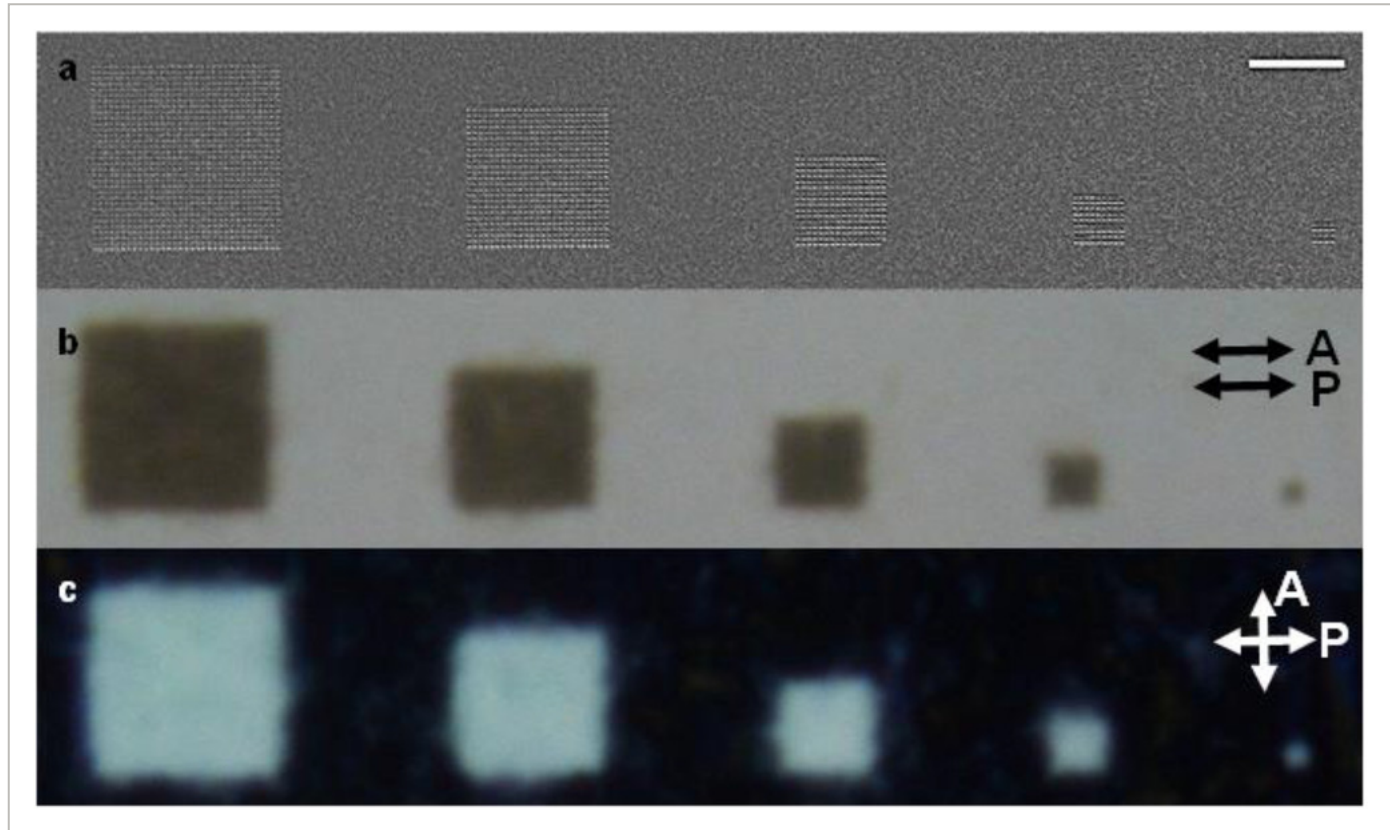


Figure 8

[Open in figure viewer](#)

[PowerPoint](#)

a) SEM and b,c) POM images of five fabricated square metasurface patterns with the meta-atoms of $W/L = 1:4$. Scale bar: 10 μm .

3 Conclusion

In summary, we have synergistically merged LCs and specially designed gold metasurfaces and demonstrated multiple optical functions. On the one hand, we showed that specially designed gold metasurfaces can provide superior alignment of LCs, removing the need for an alignment layer on the metasurface. More importantly, the designed metasurfaces can provide position-dependent, micrometer-scale localized alignment. The experimentally achieved alignment resolution is as high as 2 μm . On the other hand, the aligned LCs are also able to actively

active modulation of the plasmonic resonances of gold metasurfaces. The active modulation of the plasmonic

resonances can be achieved by either rotating the polarizer/analyzer or applying an electric field. By switching the alignment of the LC molecules, the longitudinal and transverse plasmonic resonances of the gold metasurfaces can be interchanged. The synergistic mergence of LCs and metasurfaces can enable a designed optical device to work simultaneously in both visible and NIR ranges, which is highly promising for multiple applications at one time, such as high-resolution display, modulation, anti-counterfeiting, beam deflection, LiDAR, etc.

4 Experimental Section

Nanofabrication

The gold metasurfaces were fabricated on an ITO-coated glass substrate using electron-beam lithography (EBL), followed by metal evaporation and lift-off process. The ITO-coated glass substrate was cleaned with acetone and isopropyl alcohol (IPA) in an ultrasonic bath. To pattern the gold metasurfaces via EBL, a positive electron beam resist (AR-P 6200.09) was spin-coated on the ITO-coated glass substrate to form a resist layer with a thickness of 150 nm. Following that, a thin layer of conductive solution (AR-PC 5090.02) was further spin-coated to prevent the charge accumulation effect during subsequent electron beam exposure. Prebaking was carried out at 150 °C for 2 min. EBL was carried out with a system (nB5, Nano beam). The current and voltage used were 4 nA and 80 kV, respectively. Each pattern exposed subfield was $20 \times 20 \mu\text{m}^2$. The pattern development was done in AR 600–546 for 60 s. After that, in an electron beam evaporation system (TF-500, HHV), a 2 nm chrome adhesion layer and a 50-nm-thick gold film were subsequently deposited on the resist pattern. The evaporation rate during the deposition process were controlled to be $\approx 0.4 \text{ \AA s}^{-1}$ with the vacuum level of 5×10^{-6} Torr inside the evaporator chamber. Finally, the gold metasurfaces were achieved after a lift-off process in the resist remover (AR 600–71).

LC Cell Fabrication

The PI (DL-5260, DALTON) solution was spin-coated on another cleaned ITO-coated glass substrate and then baked in an oven at 200 °C for 6 h. The measured thickness of the PI layer was 100 nm. Then the PI layer was rubbed using a rubbing machine (LHC-MC-V1, HCPE). Two pieces of the ITO-coated glass substrates, one with the gold metasurfaces and the other one with the rubbed PI alignment layer, were assembled to form a TN LC cell with the optical adhesive NOA65. The cell gap was controlled to be 5 μm using the ball spacer. Finally, the LCs (E7) were injected into the cell through the capillary action at the isotropic temperature of 65 °C and then slowly cooled down to the room temperature.

Characterization and Measurement

The surface morphologies of as-prepared gold metasurfaces were investigated by the field-loading [MathJax]/jax/output/HTML-CSS/fonts/STIX-Web/Main/Regular/Main.js acceleration voltage of 5 kV. The

optical spectra measurements of the samples were performed using a UV-vis-NIR microspectrophotometer (CRAIC technologies Inc.) with a 75 W broadband Xenon source. Transmittance and reflectance spectra were measured using a bare ITO-coated glass substrate and a silver mirror as the reference, respectively. The probe light beam was focused onto the sample surface to have a detecting area of $73.9 \times 73.9 \mu\text{m}^2$ using a $10\times$ objective lens combined with a variable aperture. A polarized optical microscope (POM, Nikon Eclipse, Ci POL) was used to check the LC alignment and textures. A CCD camera (Nikon DS-Fi2) mounted on the POM was used for optical image acquisition. The electro-optical characteristics of the TN cell were measured using a 633 nm He-Ne laser (Research Electro-Optics Inc.), a photodetector (PM100A, Thorlabs), and a function generator (DG4102, Rigol). Upon applied a driving voltage with a square-wave form and a frequency of 1 kHz using a power amplifier (PZD350A, Trek), the TN cell was studied under two crossed polarizers. The response time was retrieved using an oscilloscope (DPO2024, Tektronix).

Numerical Simulation

The refractive index of the gold thin film was obtained using ellipsometry (Horibar, UVISEL) in the spectral range of 400–2000 nm. The optical fields of the gold metasurfaces were calculated using the finite-difference time-domain (FDTD) method. A unit cell of the metasurface was simulated with periodic (x - and y -directions) and perfectly matched layer (PML) (z -direction) boundary conditions. A plane wave with its polarization either in the x - or y -direction was normally incident from the bottom, reaching the ITO-coated glass substrate first. A series of simulations were carried out with the two polarization directions for the different sets of width-to-length ratios of gold meta-atoms. Auto-uniform meshing with the finest mesh of 2 nm was used to achieve the accurate results. The plane wave source was selected with the wavelengths ranging from 400 to 2000 nm. Three power monitors were separately located 5 nm and ± 1 mm above the Au metasurface to collect electric field intensity and transmitted/reflected optical signals, respectively.

Acknowledgements

This work was supported in part by National Natural Science Foundation of China (Grant Nos. 62075093 and 61805113), China Postdoctoral Science Foundation (2020M672697), Guangdong Innovative and Entrepreneurial Research Team Program (Grant No. 2017ZT07C071), Natural Science Foundation of Guangdong Province (Grant Nos. 2018A030310224 and 2019A1515110864), Shenzhen Science and Technology Innovation Commission (Grant Nos. JCYJ20180305180635082, GJHZ20180928155207206, and JCYJ20170817111349280), and Open Fund of State Key Laboratory of Applied Optics (Grant No. SKLAO-201904). The authors also acknowledge the assistance of SUSTech Core Research Facilities.

Loading [MathJax]/jax/output/HTML-CSS/fonts/STIX-Web/Main/Regular/Main.js

Conflict of Interest

The authors declare no conflict of interest.

Open Research



Data Availability Statement

The data that support the findings of this study are available from the corresponding author upon reasonable request.

Supporting Information



Filename	Description
Ipor202100396-sup-0001-SuppMat.pdf 568.6 KB	Supporting Information
Ipor202100396-sup-0002-SuppVideo1.mp4 961.1 KB	Supporting Information
Ipor202100396-sup-0003-SuppVideo2.mp4 679.6 KB	Supporting Information
Ipor202100396-sup-0004-SuppVideo3.mp4 2.6 MB	Supporting Information
Ipor202100396-sup-0005-SuppVideo4.mp4 1.8 MB	Supporting Information

Please note: The publisher is not responsible for the content or functionality of any supporting information supplied by the authors. Any queries (other than missing content) should be directed to the corresponding author for the article.

References



- 1 Y. Zhao, M. A. Belkin, A. Alù, *Nat. Commun.* 2012, **3**, 870.

[Crossref](#) | [CAS](#) | [PubMed](#) | [Web of Science®](#) | [Google Scholar](#) | [Get it @ NYU](#)

Loading [MathJax]/jax/output/HTML-CSS/fonts/STIX-Web/Main/Regular/Main.js

2 J. P. Balthasar Mueller, N. A. Rubin, R. C. Devlin, B. Groever, F. Capasso, *Phys. Rev. Lett.* 2017, **118**, 113901.

[Crossref](#) | [CAS](#) | [PubMed](#) | [Web of Science®](#) | [Google Scholar](#) | [Get it @ NYU](#)

3 H. Kurosawa, B. Choi, Y. Sugimoto, M. Iwanaga, *Opt. Express* 2017, **25**, 4446.

[Crossref](#) | [CAS](#) | [PubMed](#) | [Web of Science®](#) | [Google Scholar](#) | [Get it @ NYU](#)

4 Y. ChenJ. Gao, X. Yang, *Laser Photonics Rev.* 2018, **12**, 1800198.

[Wiley Online Library](#) | [Web of Science®](#) | [Google Scholar](#) | [Get it @ NYU](#)

5 A. H. Dorrah, N. A. Rubin, A. Zaidi, M. Tamagnone, F. Capasso, *Nat. Photonics* 2021, **15**, 287.

[Crossref](#) | [CAS](#) | [Web of Science®](#) | [Google Scholar](#) | [Get it @ NYU](#)

6 L. Liu, X. Zhang, M. Kenney, X. Su, N. Xu, C. Ouyang, Y. Shi, J. Han, W. Zhang, S. Zhang, *Adv. Mater.* 2014, **26**, 5031.

[Wiley Online Library](#) | [CAS](#) | [PubMed](#) | [Web of Science®](#) | [Google Scholar](#) | [Get it @ NYU](#)

7 A. C. Overvig, S. Shrestha, S. C. Malek, M. Lu, A. Stein, C. Zheng, N. Yu, *Light: Sci. Appl.* 2019, **8**, 92.

[Crossref](#) | [PubMed](#) | [Web of Science®](#) | [Google Scholar](#) | [Get it @ NYU](#)

8 F. Aieta, M. A. Kats, P. Genevet, F. Capasso, *Science* 2015, **347**, 1342.

[Crossref](#) | [CAS](#) | [PubMed](#) | [Web of Science®](#) | [Google Scholar](#) | [Get it @ NYU](#)

9 Z. Li, M.-H. Kim, C. Wang, Z. Han, S. Shrestha, A. C. Overvig, M. Lu, A. Stein, A. M. Agarwal, M. Lončar, N. Yu, *Nat. Nanotechnol.* 2017, **12**, 675.

[Crossref](#) | [CAS](#) | [PubMed](#) | [Web of Science®](#) | [Google Scholar](#) | [Get it @ NYU](#)

10 G. Zheng, H. Mühlenbernd, M. Kenney, G. Li, T. Zentgraf, S. Zhang, *Nat. Nanotechnol.* 2015, **10**, 308.

[Crossref](#) | [CAS](#) | [PubMed](#) | [Web of Science®](#) | [Google Scholar](#) | [Get it @ NYU](#)

11 X. Ni, A. V. Kildishev, V. M. Shalaev, *Nat. Commun.* 2013, **4**, 2807.

[Crossref](#) | [Web of Science®](#) | [Google Scholar](#) | [Get it @ NYU](#)

12 M. Khorasaninejad, F. Aieta, P. Kanhaiya, M. A. Kats, P. Genevet, D. Rousso, F. Capasso, *Nano Lett.* 2015, **15**, 5358.

[Crossref](#) | [CAS](#) | [PubMed](#) | [Web of Science®](#) | [Google Scholar](#) | [Get it @ NYU](#)

13 S. Sun, W. Yang, C. Zhang, J. Jing, Y. Gao, X. Yu, Q. Song, S. Xiao, *ACS Nano* 2018, **12**, 2151.

[Crossref](#) | [CAS](#) | [PubMed](#) | [Web of Science®](#) | [Google Scholar](#) | [Get it @ NYU](#)

Loading [MathJax]/jax/output/HTML-CSS/fonts/STIX-Web/Main/Regular/Main.js

14 Q. He, S. Sun, L. Zhou, *Research* 2019, **2019**, 1849272.

[CAS](#) | [PubMed](#) | [Google Scholar](#) | [Get it @ NYU](#)

15 P. P. Iyer, N. A. Butakov, J. A. Schuller, *ACS Photonics* 2015, **2**, 1077.

[Crossref](#) | [CAS](#) | [Web of Science®](#) | [Google Scholar](#) | [Get it @ NYU](#)

16 C.-H. Lee, M.-K. Seo, *Opt. Lett.* 2020, **45**, 2502.

[Crossref](#) | [CAS](#) | [PubMed](#) | [Web of Science®](#) | [Google Scholar](#) | [Get it @ NYU](#)

17 Z. Wang, T. Li, A. Soman, D. Mao, T. Kananen, T. Gu, *Nat. Commun.* 2019, **10**, 3547.

[Crossref](#) | [PubMed](#) | [Web of Science®](#) | [Google Scholar](#) | [Get it @ NYU](#)

18 Y. Guo, Y. Huang, X. Li, M. Pu, P. Gao, J. Jin, X. Ma, X. Luo, *Adv. Opt. Mater.* 2019, **7**, 1900503.

[Wiley Online Library](#) | [Web of Science®](#) | [Google Scholar](#) | [Get it @ NYU](#)

19 A. Komar, R. Paniagua-Domínguez, A. Miroshnichenko, Y. F. Yu, Y. S. Kivshar, A. I. Kuznetsov, D. Neshev, *ACS Photonics* 2018, **5**, 1742.

[Crossref](#) | [CAS](#) | [Web of Science®](#) | [Google Scholar](#) | [Get it @ NYU](#)

20 Y. J. Liu, Q. Z. Hao, J. S. T. Smalley, J. Liou, I. C. Khoo, T. J. Huang, *Appl. Phys. Lett.* 2010, **97**, 091101.

[Crossref](#) | [CAS](#) | [Web of Science®](#) | [Google Scholar](#) | [Get it @ NYU](#)

21 Y. J. Liu, E. S. P. Leong, B. Wang, J. H. Teng, *Plasmonics* 2011, **6**, 659.

[Crossref](#) | [CAS](#) | [Web of Science®](#) | [Google Scholar](#) | [Get it @ NYU](#)

22 Y. J. Liu, G. Y. Si, E. S. P. Leong, N. Xiang, A. J. Danner, J. H. Teng, *Adv. Mater.* 2012, **24**, OP131.

[Wiley Online Library](#) | [CAS](#) | [PubMed](#) | [Web of Science®](#) | [Google Scholar](#) | [Get it @ NYU](#)

23 G. Y. Si, Y. H. Zhao, E. S. P. Leong, Y. J. Liu, *Materials* 2014, **7**, 1296.

[Crossref](#) | [CAS](#) | [PubMed](#) | [Web of Science®](#) | [Google Scholar](#) | [Get it @ NYU](#)

24 M. Decker, C. Kremers, A. Minovich, I. Staude, A. E. Miroshnichenko, D. Chigrin, D. N. Neshev, C. Jagadish, Y. S. Kivshar, *Opt. Express* 2013, **21**, 8879.

[Crossref](#) | [PubMed](#) | [Web of Science®](#) | [Google Scholar](#) | [Get it @ NYU](#)

25 J. Wu, Z. Shen, S. Ge, B. Chen, Z. Shen, T. Wang, C. Zhang, W. Hu, K. Fan, W. Padilla, Y. Lu, B. Jin, J. Chen, P. Wu, *Appl. Phys. Lett.* 2020, **116**, 131104.

[Crossref](#) | [CAS](#) | [Web of Science®](#) | [Google Scholar](#) | [Get it @ NYU](#)

27 B. Atorf, H. Mühlenbernd, T. Zentgraf, H. Kitzerow, *Opt. Express* 2020, **28**, 8898.

[Crossref](#) | [PubMed](#) | [Web of Science®](#) | [Google Scholar](#) | [Get it @ NYU](#)

28 Y. Liu, J. Song, W. Zhao, X. Ren, Q. Cheng, X. Luo, N. X. Fang, R. Hu, *Nanophotonics* 2020, **9**, 855.

[Crossref](#) | [Web of Science®](#) | [Google Scholar](#) | [Get it @ NYU](#)

29 J. Li, P. Yu, S. Zhang, N. Liu, *Nat. Commun.* 2020, **11**, 3574.

[Crossref](#) | [PubMed](#) | [Web of Science®](#) | [Google Scholar](#) | [Get it @ NYU](#)

30 A. M. Shaltout, V. M. Shalaev, M. L. Brongersma, *Science* 2019, **364**, eaat3100.

[Crossref](#) | [CAS](#) | [PubMed](#) | [Web of Science®](#) | [Google Scholar](#) | [Get it @ NYU](#)

31 C. Zou, A. Komar, S. Fasold, J. Bohn, A. A. Muravsky, A. A. Murauski, T. Pertsch, D. N. Neshev, I. Staude, *ACS Photonics* 2019, **6**, 1533.

[Crossref](#) | [CAS](#) | [Web of Science®](#) | [Google Scholar](#) | [Get it @ NYU](#)

32 Z. Ma, X. Meng, X. Liu, G. Si, Y. J. Liu, *Nanomaterials* 2018, **8**, 871.

[Crossref](#) | [Web of Science®](#) | [Google Scholar](#) | [Get it @ NYU](#)

33 M. Sharma, T. Ellenbogen, *Laser Photonics Rev.* 2020, **14**, 2000253.

[Wiley Online Library](#) | [CAS](#) | [Web of Science®](#) | [Google Scholar](#) | [Get it @ NYU](#)

34 M. Jiang, Y. Guo, H. Yu, Z. Zhou, T. Turiv, O. D. Lavrentovich, Q. Wei, *Adv. Mater.* 2019, **31**, 1808028.

[Wiley Online Library](#) | [Web of Science®](#) | [Google Scholar](#) | [Get it @ NYU](#)

35 H. Yu, M. Jiang, Y. Guo, T. Turiv, W. Lu, V. Ray, O. D. Lavrentovich, Q. Wei, *Adv. Opt. Mater.* 2019, **7**, 1900117.

[Wiley Online Library](#) | [Web of Science®](#) | [Google Scholar](#) | [Get it @ NYU](#)

36 O. Buchnev, N. Podoliak, M. Kaczmarek, N. I. Zheludev, V. A. Fedotov, *Adv. Opt. Mater.* 2015, **3**, 674.

[Wiley Online Library](#) | [CAS](#) | [Web of Science®](#) | [Google Scholar](#) | [Get it @ NYU](#)

37 A. Minovich, J. Farnell, D. N. Neshev, I. McKerracher, F. Karouta, J. Tian, D. A. Powell, I. V. Shadrivov, H. H. Tan, C. Jagadish, Y. S. Kivshar, *Appl. Phys. Lett.* 2012, **100**, 121113.

[Crossref](#) | [CAS](#) | [Web of Science®](#) | [Google Scholar](#) | [Get it @ NYU](#)

38 J. Sautter, I. Staude, M. Decker, E. Rusak, D. N. Neshev, I. Brener, Y. S. Kivshar, *ACS Nano* 2015, **9**, 4308.

[Crossref](#) | [CAS](#) | [PubMed](#) | [Web of Science®](#) | [Google Scholar](#) | [Get it @ NYU](#)

Loading [MathJax]/jax/output/HTML-CSS/fonts/STIX-Web/Main/Regular/Main.js

39 S.-Q. Li, X. Xu, R. M. Veetil, V. Valuckas, R. Paniagua-Domínguez, A. I. Kuznetsov, *Science* 2019, **364**, 1087.

[Crossref](#) | [CAS](#) | [PubMed](#) | [Web of Science®](#) | [Google Scholar](#) | [Get it @ NYU](#)

40 O. Buchnev, J. Y. Ou, M. Kaczmarek, N. I. Zheludev, V. A. Fedotov, *Opt. Express* 2013, **21**, 1633.

[Crossref](#) | [CAS](#) | [PubMed](#) | [Web of Science®](#) | [Google Scholar](#) | [Get it @ NYU](#)

41 O. Buchnev, N. Podoliak, V. A. Fedotov, *J. Mol. Liq.* 2018, **267**, 411.

[Crossref](#) | [CAS](#) | [Web of Science®](#) | [Google Scholar](#) | [Get it @ NYU](#)

42 R. Bartholomew, C. Williams, A. Khan, R. Bowman, T. Wilkinson, *Opt. Lett.* 2017, **42**, 2810.

[Crossref](#) | [CAS](#) | [PubMed](#) | [Web of Science®](#) | [Google Scholar](#) | [Get it @ NYU](#)

43 C. L. Haynes, R. P. Van Duyne, *Nano Lett.* 2003, **3**, 939.

[Crossref](#) | [CAS](#) | [Web of Science®](#) | [Google Scholar](#) | [Get it @ NYU](#)

44 A. Agharazy Dormeny, P. Abedini Sohi, M. Kahrizi, *Results Phys.* 2020, **16**, 102869.

[Crossref](#) | [Web of Science®](#) | [Google Scholar](#) | [Get it @ NYU](#)

45 R. Gans, *Ann. Phys.* 1912, **342**, 881.

[Wiley Online Library](#) | [Google Scholar](#) | [Get it @ NYU](#)

46 M. Hu, J. Chen, Z. Y. Li, L. Au, G. V. Hartland, X. Li, M. Marquez, Y. Xia, *Chem. Soc. Rev.* 2006, **35**, 1084.

[Crossref](#) | [CAS](#) | [PubMed](#) | [Web of Science®](#) | [Google Scholar](#) | [Get it @ NYU](#)

47 Y. J. Liu, W. W. Loh, E. S. P. Leong, T. S. Kustandi, X. W. Sun, J. H. Teng, *Nanotechnology* 2012, **23**, 465302.

[Crossref](#) | [PubMed](#) | [Web of Science®](#) | [Google Scholar](#) | [Get it @ NYU](#)

48 G. Si, E. S. P. Leong, X. Jiang, J. Lv, J. Lin, H. Dai, Y. J. Liu, *Phys. Chem. Chem. Phys.* 2015, **17**, 13223.

[Crossref](#) | [CAS](#) | [PubMed](#) | [Web of Science®](#) | [Google Scholar](#) | [Get it @ NYU](#)

49 V. Kumar, Z. Q. Ye, H. D. Jiang, Y. Shi, K. Li, D. Gérard, D. Luo, Q. Q. Mu, Y. J. Liu, *ACS Appl. Electron. Mater.* 2020, **2**, 2017.

[Crossref](#) | [CAS](#) | [Google Scholar](#) | [Get it @ NYU](#)

50 C.-T. Wang, H.-H. Hou, P.-C. Chang, C.-C. Li, H.-C. Jau, Y.-J. Hung, T.-H. Lin, *Opt. Express* 2016, **24**, 22892.

[Crossref](#) | [CAS](#) | [PubMed](#) | [Web of Science®](#) | [Google Scholar](#) | [Get it @ NYU](#)

Loading [MathJax]/jax/output/HTML-CSS/fonts/STIX-Web/Main/Regular/Main.js

Citing Literature

[Download PDF](#)

About Wiley Online Library

[Privacy Policy](#)[Terms of Use](#)[About Cookies](#)[Manage Cookies](#)[Accessibility](#)[Wiley Research DE&I Statement and Publishing Policies](#)

Help & Support

[Contact Us](#)[Training and Support](#)[DMCA & Reporting Piracy](#)

Opportunities

[Subscription Agents](#)[Advertisers & Corporate Partners](#)

Connect with Wiley

[The Wiley Network](#)[Wiley Press Room](#)

Copyright © 1999-2022 John Wiley & Sons, Inc. All rights reserved

Loading [MathJax]/jax/output/HTML-CSS/fonts/STIX-Web/Main/Regular/Main.js